

# An efficient iterative method for reconstructing surface from point clouds

Dong Wang<sup>a,\*</sup>

<sup>a</sup>*Department of Mathematics, University of Utah, Salt Lake City, UT, 84112 USA.*

---

## Abstract

Surface reconstruction from point clouds is a fundamental step in many applications in computer vision. In this paper, we develop an efficient iterative method on a variational model for the surface reconstruction from point clouds. The surface is implicitly represented by indicator functions and the energy functional is then approximated based on such representations using heat kernel convolutions. We then develop a novel iterative method to minimize the approximate energy and prove the energy decaying property during each iteration. We then use asymptotic expansion to give a connection between the proposed algorithm and interface dynamics. Extensive numerical experiments are performed in both 2- and 3- dimensional Euclidean spaces to show that the proposed method is simple, efficient, and accurate.

*Keywords:* iterative method, thresholding, surface reconstruction, point cloud

---

## 1. Introduction

The problem of reconstructing surfaces from point clouds has attracted tremendous attention for the past decades [1]. Point clouds are usually obtained using optical measuring devices such as laser scanners. It is a fundamental step in many applications such as computer graphics [2, 3], medical imaging [4], manufacturing applications [5], and many others [1, 6].

In this paper, we consider the reconstruction of  $n - 1$ -dimensional manifold from a point cloud  $\mathcal{C} \in \mathbb{R}^n$  (for example, a curve in  $\mathbb{R}^2$  or a surface in  $\mathbb{R}^3$ ). To be specific, motivated from [7], we consider the following optimization problem:

$$\Gamma^* = \min_{\Gamma} E(\Gamma) := \left( \int_{\Gamma} |d|^p ds \right)^{\frac{1}{p}} \quad (1)$$

where  $d(\mathbf{x}) = \min_{\mathbf{y} \in \mathcal{C}} |\mathbf{x} - \mathbf{y}|$  is the distance from any point  $\mathbf{x} \in \mathbb{R}^n$  to the point cloud  $\mathcal{C}$ ,  $p$  is a positive number,  $ds$  is the line/surface integral element, and  $\Gamma^*$  is the surface to be reconstructed.

The goal of (1) is to find an optimal surface in the sense of minimizing the  $p$ -norm of the distance function on the surface. In the continuous limit, when  $d(x)$  is the distance function to a smooth surface  $\Gamma_0$ ,

---

\*Corresponding author

*Email address:* [dwang@math.utah.edu](mailto:dwang@math.utah.edu) (Dong Wang)

10 it is easy to see that there are two global minimizers (*i.e.*;  $\Gamma = \Gamma_0$  and  $\Gamma = \emptyset$ ). However, in general and  
11 practical situations,  $\mathcal{C}$  is a discrete set and may have noise or missing data. The problem is then interesting  
12 and complicated. In this case, the only one global minimizer is the trivial solution  $\Gamma = \emptyset$  and the nontrivial  
13 local minimizer is more interesting.

14 There have been many successful developments along the direction on the surface reconstruction from  
15 point cloud using a variational approach: mainly on different objective functionals and numerical methods;  
16 for instance, the Poisson surface reconstruction method [8], moving least square projections [9], recon-  
17 structing surfaces using anisotropic radius basis functions [10], polygonal surface reconstruction [11], and  
18 reconstruction using image segmentation formulations [12]. Besides these, there are many data driven ap-  
19 proaches developed for surface reconstruction with priors for considering sampling density, level of noise,  
20 missing alignment, local surface smoothness, volumetric smoothness, absence of boundaries, symmetries,  
21 shape primitives, or global regularity. We refer to [6] and references therein for a detailed survey on data-  
22 driven approaches.

23 In this paper, we use the indicator function to implicitly represent the surface and approximate the  
24 energy in (1) using the indicator functions. Based on the new approximation, we derive an unconditional  
25 stable and efficient method to minimize the approximate energy to approximate the optimized solution.

26 The method is motivated by the threshold dynamics method [13–15] for simulating the motion by mean  
27 curvature. Recently, the method is interpreted as a minimizing movement scheme of a Lyapunov functional  
28 of indicator functions in [16]. The novel derivation and interpretation in [16] can then be directly generated  
29 to multiphase mean curvature motion with arbitrary surface tensions. The method has attracted much  
30 attention due to its simplicity and unconditional stability. It has subsequently been extended to many  
31 problems, including the problem of area or volume preserving interface motion [17, 18], wetting dynamics  
32 [19, 20], image processing [21–24], target-value harmonic maps [25–28], high-order geometric motions [29],  
33 and so on.

34 Threshold dynamics method can also be generalized and extended to modeling anisotropic interface  
35 motions via constructing a specific kernel (instead of heat kernel) (see [30–32] for more details). It is obvious  
36 that the gradient flow of (1) is also an anisotropic interface motion where the anisotropy comes from varying  
37  $|d|^p$  in the domain. However, when the anisotropy is fixed in the computational domain, approaches from  
38 constructing kernels would fail.

39 In this work, we derive a novel threshold dynamics type method for the application in reconstructing  
40 surface from point clouds. We understand this as an iterative approach for minimizing a given surface energy.  
41 Also, we perform asymptotic expansions to formally analysis the anisotropic dynamics of the interface during  
42 each iteration, to build a connection between the method and interface dynamics.

43 The rest of this paper is organized as follows. In Section 2, we introduce new approximations of the energy,  
44 derive the numerical method based on the approximation, and prove the unconditional stability property

45 of the method. We discuss some interpretations of dynamics of the interface in Section 3. In Section 4,  
 46 we provide an accelerated version of the proposed algorithms. In Section 5, we describe the numerical  
 47 implementation and illustrate the performance of the method using extensive numerical experiments. We  
 48 draw some conclusions and discussions in Section 6.

## 49 2. Derivation of the method

### 50 2.1. Approximation of the energy in (1).

In this paper, since we focus on the codimension 1 interface (*e.g.*, a closed curve in  $\mathbb{R}^2$ , a surface in  $\mathbb{R}^3$ ,  
 or higher dimensions), we use indicator functions to implicitly represent the interface. That is, we denote

$$u(x) = \begin{cases} 1 & \text{if } \mathbf{x} \in \Omega_\Gamma \\ 0 & \text{otherwise} \end{cases} \quad (2)$$

51 where  $\Omega_\Gamma$  is the domain bounded by an interface  $\Gamma$ .

Under this representation, as shown in [33], as  $\tau \searrow 0$ , the boundary integral  $\int_\Gamma |d|^p ds$  is approximated  
 by a short time heat flow (*i.e.*; Gaussian convolution):

$$\int_\Gamma |d|^p ds \approx \sqrt{\frac{\pi}{\tau}} \int_{\mathbb{R}^n} |d|^p u G_\tau * (1 - u) d\mathbf{x}, \quad (3)$$

or

$$\int_\Gamma |d|^p ds \approx \sqrt{\frac{\pi}{\tau}} \int_{\mathbb{R}^n} |d|^p (1 - u) G_\tau * u d\mathbf{x} \quad (4)$$

where

$$G_\tau(\mathbf{x}) = \frac{1}{(4\pi\tau)^{n/2}} \exp\left(-\frac{|\mathbf{x}|^2}{4\tau}\right),$$

\* denotes the convolution, and  $\tau$  is a free parameter. To keep the symmetry of the formula with respect to  
 $u$  and  $1 - u$ , we approximate  $\int_\Gamma |d|^p ds$  by  $E^\tau(u)$ :

$$E^\tau(u) = \frac{1}{2} \sqrt{\frac{\pi}{\tau}} \left( \int_{\mathbb{R}^n} |d|^p u G_\tau * (1 - u) d\mathbf{x} + \int_{\mathbb{R}^n} |d|^p (1 - u) G_\tau * u d\mathbf{x} \right) \quad (5)$$

or

$$E^\tau(u) = \sqrt{\frac{\pi}{\tau}} \int_{\mathbb{R}^n} |d|^{\frac{p}{2}} u G_\tau * \left( |d|^{\frac{p}{2}} (1 - u) \right) d\mathbf{x}. \quad (6)$$

52 We note that in the special case when  $|d|^p = 1$ , the formula reduces to the perimeter or the surface area.  
 53 It can be used to model multiphase motion with arbitrary surface tensions [16]. The convergence of (6) as  
 54  $\tau \searrow 0$  is rigorously proved in [34] when they study wetting dynamics with surfactant.

Now, we arrive at the following problem: finding  $u^{\tau,*}$  such that

$$u^{\tau,*} = \arg \min_{u \in \mathcal{B}} E^\tau(u) \quad (7)$$

where

$$\mathcal{B} := \{u \in BV(\Omega, \mathbb{R}) \mid u = \{0, 1\}\}$$

55 and  $BV(\Omega, \mathbb{R})$  denotes the bounded-variation functional space.

56 *2.2. Derivation of the method based on (5).*

In this section, we iteratively solve (7). We first note that problem (7) is a minimization problem of a functional on a nonconvex set  $\mathcal{B}$ . Using the relaxation approach in [16], we relax this problem to an equivalent problem: finding  $u^{\tau, \star}$  such that

$$u^{\tau, \star} = \arg \min_{u \in \mathcal{K}} E^\tau(u) \quad (8)$$

where

$$\mathcal{K} := \{u \in BV(\Omega, \mathbb{R}) \mid u \in [0, 1]\}.$$

57 The equivalence between (7) and (8) is guaranteed in the following lemma.

**Lemma 2.1.** *Problem 7 is equivalent to problem 8. That is,*

$$\arg \min_{u \in \mathcal{B}} E^\tau(u) = \arg \min_{u \in \mathcal{K}} E^\tau(u).$$

*Proof.* It is easy to see that

$$\min_{u \in \mathcal{K}} E^\tau(u) \leq \min_{u \in \mathcal{B}} E^\tau(u)$$

58 from the fact that  $\mathcal{B} \subsetneq \mathcal{K}$ .

To finish the proof, we need only to prove

$$\arg \min_{u \in \mathcal{K}} E^\tau(u) \in \mathcal{B}.$$

Assume it is not true and the minimizer is  $u^*$ , then there exists a set  $A \subset \Omega$  with nonzero measure and  $c > 0$  such that

$$u^*(x) \in (c, 1 - c), \quad \forall x \in A.$$

Denote  $u^t = u^* + t\chi_A$  where  $\chi_A$  is the indicator function of  $A$ , we have  $u^t \in \mathcal{K}$  for any  $|t| < c$ . Direct computation yields

$$\frac{d^2 E^\tau(u^t)}{dt^2} = -2\sqrt{\frac{\pi}{\tau}} \int_{\mathbb{R}^n} |d|^p \chi_A G_\tau * \chi_A \, dx.$$

59 Because  $|d|^p \geq 0$  and  $|d|^p = 0$  only on a set with zero measure, we have  $\frac{d^2 E^\tau(u^t)}{dt^2} < 0$ , especially at  $t = 0$   
60 (*i.e.*,  $u^*$ ). This contradicts with the assumption that  $u^*$  is a minimizer.

61 Therefore, we have that the minimizer of  $\min_{u \in \mathcal{K}} E^\tau(u)$  must be attained in  $\mathcal{B}$ . □

Now, we use an iterative method to solve (8). Without loss of generality, assume the  $k$ -th iteration is known, we find  $k + 1$ -th iteration as follows. At the  $k$ -th iteration  $u^k$ , we compute the linearization of  $E^\tau(u)$  at  $u^k$ :

$$L^\tau(u, u^k) = \frac{1}{2} \sqrt{\frac{\pi}{\tau}} \int_{\mathbb{R}^n} u \varphi^k d\mathbf{x} \quad (9)$$

where

$$\varphi^k = |d|^p G_\tau * (1 - 2u^k) + G_\tau * (|d|^p (1 - 2u^k)).$$

Based on the sequential linear programming, we then compute the  $k + 1$ -th iteration  $u^{k+1}$  by solving the following linearized problem:

$$u^{k+1} = \arg \min_{u \in \mathcal{K}} L^\tau(u, u^k). \quad (10)$$

Since  $u$  only takes value in  $[0, 1]$  (*i.e.*, a bounded set), the minimization problem (10) can be solved point-wisely. That is, at each point  $\mathbf{x}$ ,

$$u^{k+1}(\mathbf{x}) = \arg \min_{u(\mathbf{x}) \in [0, 1]} u(\mathbf{x}) \varphi^k(\mathbf{x}).$$

This is exactly solved via the following thresholding step:

$$u^{k+1}(\mathbf{x}) = \begin{cases} 1, & \text{if } \varphi^k(\mathbf{x}) < 0, \\ 0, & \text{otherwise.} \end{cases}$$

62 The algorithm is summarized into Algorithm 1.

---

**Algorithm 1:** The iterative method for approximating minimizers of (5).

---

**Input:**  $\Omega$ : computational domain;  $d$ : distance function to the point cloud;  $\tau > 0$ ; and  $u^0 \in \mathcal{B}$ .

**Output:**  $u^* \in \mathcal{B}$ .

**while** *not converged* **do**

1. For the fixed  $u^k$ , compute

$$\varphi^k(\mathbf{x}) = |d|^p G_\tau * (1 - 2u^k) + G_\tau * (|d|^p (1 - 2u^k)).$$

2. Set

$$u^{k+1}(\mathbf{x}) = \begin{cases} 1 & \text{if } \varphi^k(\mathbf{x}) \leq 0, \\ 0 & \text{otherwise.} \end{cases}$$


---

63 *Remark 2.2.* The criteria for “convergence” in all proposed algorithms is that  $u^{k+1}(\bar{\mathbf{x}}) = u^k(\bar{\mathbf{x}})$  on each grid  
64 point  $\bar{\mathbf{x}}$  in the discretized domain. In other words, the value of  $u$  at no grid point is changing (from 1 to 0  
65 or 0 to 1).

66 2.3. Derivation of the method based on (6).

67 Similar to the derivation in Algorithm 1, we use the same relaxation and linearization approach to derive  
68 another unconditional stable method in Algorithm 2. The details are omitted here.

---

**Algorithm 2:** The iterative method for approximating minimizers of (6).

---

**Input:**  $\Omega$ : computational domain;  $d$ : distance function to the point cloud;  $\tau > 0$ ; and  $u^0 \in \mathcal{B}$ .

**Output:**  $u^* \in \mathcal{B}$ .

**while** *not converged* **do**

1. For the fixed  $u^k$ , compute

$$\varphi^k(\mathbf{x}) = G_\tau * \left( |d|^{\frac{p}{2}} (1 - 2u^k) \right).$$

2. Set

$$u^{k+1}(\mathbf{x}) = \begin{cases} 1 & \text{if } \varphi^k(\mathbf{x}) \leq 0, \\ 0 & \text{otherwise.} \end{cases}$$


---

69 *Remark 2.3.* We remark here that, at each iteration, the computational complexity of Algorithm 2 is about  
70 the half of the computational complexity of Algorithm 1 because only one convolution needs to be computed.

71 As for Algorithm 2, we discuss the stability of the method in the sense of the monotonicity of the  
72 approximate energy (6) (i.e.;  $E^\tau(u^{k+1}) \leq E^\tau(u^k)$ ).

**Theorem 2.4.** *Suppose  $u^k$  ( $k = 1, 2, \dots$ ) are computed from Algorithm 2, we have*

$$E^\tau(u^{k+1}) \leq E^\tau(u^k)$$

73 *with  $E^\tau(u)$  being defined in (6).*

*Proof.* As for  $E^\tau(u)$  defined in (6), the linearization of  $E^\tau(u)$  at  $u^k$  is defined by:

$$L^\tau(u, u^k) = \sqrt{\frac{\pi}{\tau}} \int_{\mathbb{R}^n} |d|^{\frac{p}{2}} u G_\tau * (1 - 2u^k) \, d\mathbf{x}.$$

Note that we have

$$E^\tau(u^k) = L^\tau(u^k, u^k) + \sqrt{\frac{\pi}{\tau}} \int_{\mathbb{R}^n} |d|^{\frac{p}{2}} u^k G_\tau * \left( |d|^{\frac{p}{2}} u^k \right) \, d\mathbf{x}$$

and

$$E^\tau(u^{k+1}) = L^\tau(u^{k+1}, u^k) + 2\sqrt{\frac{\pi}{\tau}} \int_{\mathbb{R}^n} |d|^{\frac{p}{2}} u^{k+1} G_\tau * \left( |d|^{\frac{p}{2}} u^k \right) \, d\mathbf{x} - \sqrt{\frac{\pi}{\tau}} \int_{\mathbb{R}^n} |d|^{\frac{p}{2}} u^{k+1} G_\tau * \left( |d|^{\frac{p}{2}} u^{k+1} \right) \, d\mathbf{x}.$$

Because  $u^{k+1}$  is the solution from the sequential linear programming, we have  $L^\tau(u^{k+1}, u^k) \leq L^\tau(u^k, u^k)$ .

Then, we compute

$$E^\tau(u^{k+1}) - E^\tau(u^k) = L^\tau(u^{k+1}, u^k) - L^\tau(u^k, u^k) + \mathcal{L}$$

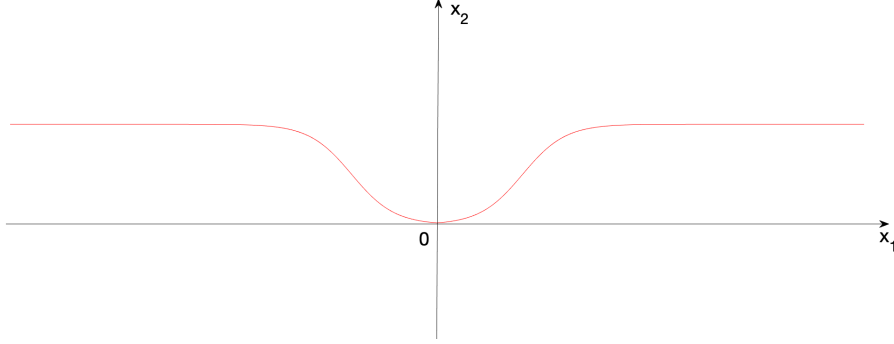


Figure 1: A diagram for the set up for the asymptotic analysis. See Section 3.

where

$$\begin{aligned} \mathcal{L} &= -\sqrt{\frac{\pi}{\tau}} \int_{\mathbb{R}^n} |d|^{\frac{p}{2}} (u^{k+1} - u^k) G_\tau * \left( |d|^{\frac{p}{2}} (u^{k+1} - u^k) \right) d\mathbf{x} \\ &= -\sqrt{\frac{\pi}{\tau}} \int_{\mathbb{R}^n} \left[ G_{\tau/2} * \left( |d|^{\frac{p}{2}} (u^{k+1} - u^k) \right) \right]^2 \leq 0. \end{aligned}$$

74 Therefore, we are led that  $E^\tau(u^{k+1}) - E^\tau(u^k) \leq 0$ . □

### 75 3. Interpretations of interface dynamics.

76 Note that, at each iteration, both Algorithm 1 and Algorithm 2 start from an indicator function and end  
77 by another indicator function, which implicitly determines a motion of a front. The free parameter  $\tau$  can  
78 be interpreted as the time step in the dynamics of the interface.

79 When  $|d|^p = 1, \forall \mathbf{x} \in \Omega$ , it is easy to see that both algorithms reduce to the original MBO method [13]  
80 where the front evolves along its normal direction by mean curvature. In this case, if there is no other  
81 constraint (*e.g.*, volume constraint), the front evolves to the unique minimizer (*i.e.*, the global minimizer  $\emptyset$ ).

82 However, when  $d(\mathbf{x})$  is varying in the space, we perform the following asymptotic expansions to compute  
83 the motion law of the front during the iterations. For the convenience, we write  $\psi = |d|^{\frac{p}{2}}$  and use an  
84 asymptotic expansion to expand  $\varphi^k(\mathbf{x})$  in Algorithm 2 with respect to a small parameter  $\tau$ . Without loss  
85 of generality, we set up the interface as that in Figure 1. Specifically, we assume that  $u^k$  is the indicator  
86 function for the region where  $x_2 \geq g(x_1)$  in Figure 1. Furthermore, we assume the point of interest is the  
87 origin and  $g'(0) = 0$ .

In the follows, we focus on expanding  $\varphi^k$  into a series with respect  $\tau$  and find zero level set of  $\phi^k(\mathbf{x})$

which corresponds to the new position of the front (according to Algorithm 2):

$$\begin{aligned}
\varphi^k(\mathbf{x}) &= G_\tau * (\psi(1 - 2u^k)) \\
&= \frac{1}{4\pi\tau} \int_{-\infty}^{\infty} \int_{-\infty}^{\infty} \exp\left(-\frac{|\mathbf{x} - \mathbf{y}|^2}{4\tau}\right) \psi(\mathbf{y})(1 - 2u^k(\mathbf{y})) \, dy_2 dy_1 \\
&= \frac{1}{4\pi\tau} \int_{-\infty}^{\infty} \int_{-\infty}^{\infty} \exp\left(-\frac{|\mathbf{x} - \mathbf{y}|^2}{4\tau}\right) \psi(\mathbf{y}) \, dy_2 dy_1 - \frac{1}{2\pi\tau} \int_{-\infty}^{\infty} \int_{g(y_1)}^{\infty} \exp\left(-\frac{|\mathbf{x} - \mathbf{y}|^2}{4\tau}\right) \psi(\mathbf{y}) \, dy_2 dy_1.
\end{aligned} \tag{11}$$

Evaluating  $\varphi^k(\mathbf{x})$  at  $(0, x_2)$  (*i.e.*; the front moves along its normal direction), we have

$$\varphi^k(0, x_2) = I_1 - I_2 \tag{12}$$

where

$$I_1 = \frac{1}{4\pi\tau} \int_{-\infty}^{\infty} \int_{-\infty}^{\infty} \exp\left(-\frac{y_1^2 + (x_2 - y_2)^2}{4\tau}\right) \psi(y_1, y_2) \, dy_2 dy_1$$

and

$$I_2 = \frac{1}{2\pi\tau} \int_{-\infty}^{\infty} \int_{g(y_1)}^{\infty} \exp\left(-\frac{y_1^2 + (x_2 - y_2)^2}{4\tau}\right) \psi(y_1, y_2) \, dy_2 dy_1.$$

Assume  $\psi(y_1, y_2)$  is smooth almost everywhere and expand  $\psi(y_1, y_2)$  into its Taylor's series around  $(0, x_2)$ :

$$\psi(y_1, y_2) = \psi_{0,0} + y_1 \psi_{1,0} + (y_2 - x_2) \psi_{0,1} + \frac{y_1^2}{2} \psi_{2,0} + \frac{(y_2 - x_2)^2}{2} \psi_{0,2} + y_1 (y_2 - x_2) \psi_{1,1} + \dots \tag{13}$$

88 where  $\psi_{m,n}$  denotes the mixed partial derivative at  $(0, x_2)$  with  $m$ -th order derivative with respect to  $y_1$  and  
89  $n$ -th order derivative with respect to  $y_2$ .

As for  $I_1$ , direct computation yields

$$\begin{aligned}
I_1 &= \frac{1}{4\pi\tau} \int_{-\infty}^{\infty} \int_{-\infty}^{\infty} \exp\left(-\frac{y_1^2 + y_2^2}{4\tau}\right) \psi(y_1, y_2 + x_2) \, dy_2 dy_1 \\
&= \sum_{m,n=0}^{\infty} \psi_{m,n} \frac{1}{4\pi\tau} \int_{-\infty}^{\infty} \int_{-\infty}^{\infty} \exp\left(-\frac{y_1^2 + y_2^2}{4\tau}\right) y_1^m y_2^n \, dy_2 dy_1 \\
&= \sum_{m,n=0}^{\infty} \psi_{m,n} \frac{1}{4\pi\tau} \int_{-\infty}^{\infty} \exp\left(-\frac{y_1^2}{4\tau}\right) y_1^m \, dy_1 \int_{-\infty}^{\infty} \exp\left(-\frac{y_2^2}{4\tau}\right) y_2^n \, dy_2 \\
&= \sum_{m,n=0}^{\infty} \psi_{m,n} \eta_{m,n}
\end{aligned} \tag{14}$$

where  $\eta_{m,n} = \xi_m \xi_n$  and

$$\xi_m = \frac{1}{2\sqrt{\pi\tau}} \int_{-\infty}^{\infty} e^{-\frac{y^2}{4\tau}} y^m \, dy$$

which can be explicitly computed:

$$\xi_m = \begin{cases} 0 & \text{if } m \text{ is odd,} \\ (m-1)!! \, 2^{m/2} \tau^{m/2} & \text{if } m \text{ is positive and even,} \\ 1 & \text{if } m = 0. \end{cases}$$

Therefore,

$$I_1 = \psi_{0,0} + 2(\psi_{2,0} + \psi_{0,2})\tau + 4(\psi_{2,2} + 3\psi_{4,0} + 3\psi_{0,4})\tau^2 + o(\tau^2).$$

As for  $I_2$ , because  $g(0) = g'(0) = 0$ , we expand  $g(y_1)$  into its Taylor's series around 0 by

$$g(y_1) = \frac{g^{(2)}}{2}y_1^2 + \frac{g^{(3)}}{6}y_1^3 + \frac{g^{(4)}}{24}y_1^4 + \dots \quad (15)$$

where  $g^{(n)}$  denotes the  $n$ -th order derivative at 0. After changing of variables,  $I_2$  is then written into

$$I_2 = II_1 - II_2 \quad (16)$$

where

$$II_1 = \frac{1}{2\pi\tau} \int_{-\infty}^{\infty} \int_0^{\infty} \exp\left(-\frac{y_1^2 + y_2^2}{4\tau}\right) \psi(y_1, y_2 + x_2) dy_2 dy_1$$

and

$$II_2 = \frac{1}{2\pi\tau} \int_{-\infty}^{\infty} \int_0^{-x_2 + \frac{g^{(2)}}{2}y_1^2 + \frac{g^{(3)}}{6}y_1^3 + \frac{g^{(4)}}{24}y_1^4 + \dots} \exp\left(-\frac{y_1^2 + y_2^2}{4\tau}\right) \psi(y_1, y_2 + x_2) dy_2 dy_1.$$

For  $II_1$ , we have

$$II_1 = \sum_{m,n=0}^{\infty} \psi_{m,n} \eta'_{m,n}$$

where  $\eta'_{m,n} = \xi_m \xi'_n$  and

$$\xi'_n = \frac{1}{\sqrt{\pi\tau}} \int_0^{\infty} e^{-\frac{y^2}{4\tau}} y^n dy$$

which can be explicitly computed as follows:

$$\xi'_n = \begin{cases} \frac{1}{\sqrt{\pi\tau}} (n-1)!! (2\tau)^{(n+1)/2} & \text{if } n \text{ is odd,} \\ \xi_n & \text{if } n \text{ is even.} \end{cases}$$

Therefore,

$$II_1 = \psi_{0,0} + \frac{2\psi_{0,1}}{\sqrt{\pi}} \tau^{1/2} + 2(\psi_{2,0} + \psi_{0,2})\tau + \frac{4(2\psi_{0,3} + \psi_{2,1})}{\sqrt{\pi}} \tau^{3/2} + 4(\psi_{2,2} + 3\psi_{4,0} + 3\psi_{0,4})\tau^2 + o(\tau^2).$$

For the computation of  $II_2$ , we further expand  $e^{-\frac{y_2^2}{4\tau}}$  into its Taylor's series and compute:

$$II_2 = \sum_{m,n=0}^{\infty} \psi_{m,n} \zeta_{m,n} \quad (17)$$

where

$$\zeta_{m,n} = \frac{1}{2\pi\tau} \int_{-\infty}^{\infty} e^{-\frac{y_1^2}{4\tau}} y_1^m \int_0^{-x_2 + \frac{g^{(2)}}{2}y_1^2 + \frac{g^{(3)}}{6}y_1^3 + \frac{g^{(4)}}{24}y_1^4 + \dots} \left( y_2^n - \frac{1}{4\tau} y_2^{n+2} + \frac{1}{32\tau^2} y_2^{n+4} + \dots \right) dy_2 dy_1. \quad (18)$$

Assume  $x_2 \sim O(\tau)$  and write  $x_2 = \tau \tilde{x}_2$  with  $\tilde{x}_2 \sim O(1)$ , then the leading orders in  $\zeta_{m,n}$  are computed:

$$\begin{cases} \zeta_{0,0} = \frac{-\tilde{x}_2}{\sqrt{\pi}} \tau^{1/2} + \frac{g^{(2)}}{\sqrt{\pi}} \tau^{1/2} + \left( \frac{g^{(4)}}{2\sqrt{\pi}} + \frac{\tilde{x}_2^3}{12\sqrt{\pi}} - \frac{g^{(2)}\tilde{x}_2}{4\sqrt{\pi}} \right) \tau^{3/2} + o(\tau^{3/2}) \\ \zeta_{1,0} = \frac{2g^{(3)}}{\sqrt{\pi}} \tau^{3/2} + o(\tau^{3/2}) \\ \zeta_{0,1} = \left( \frac{\tilde{x}_2^2}{2\sqrt{\pi}} - \frac{\tilde{x}_2 g^{(2)}}{\sqrt{\pi}} + \frac{3(g^{(2)})^2}{2\sqrt{\pi}} \right) \tau^{3/2} + o(\tau^{3/2}) \\ \zeta_{2,0} = \left( \frac{-2\tilde{x}_2}{\sqrt{\pi}} + \frac{6g^{(2)}}{\sqrt{\pi}} \right) \tau^{3/2} + o(\tau^{3/2}) \\ \zeta_{0,2} = o(\tau^{3/2}) \\ \zeta_{1,1} = o(\tau^{3/2}) \end{cases}$$

Therefore,

$$II_2 = \psi_{0,0} \left( \frac{-\tilde{x}_2}{\sqrt{\pi}} + \frac{g^{(2)}}{\sqrt{\pi}} \right) \tau^{1/2} + O(\tau^{3/2}).$$

Collecting all leading terms in  $I_1$ ,  $II_1$ , and  $II_2$  yields

$$\phi^k(0, \tilde{x}_2) = -\frac{2\psi_{0,1}}{\sqrt{\pi}} \tau^{1/2} + \psi_{0,0} \left( \frac{-\tilde{x}_2}{\sqrt{\pi}} + \frac{g^{(2)}}{\sqrt{\pi}} \right) \tau^{1/2} + O(\tau^{3/2}).$$

Set  $\phi^k(0, \tilde{x}_2) = 0$ , we then have

$$\psi_{0,0} \tilde{x}_2 = \psi_{0,0} g^{(2)} - 2\psi_{0,1}. \quad (19)$$

90 Note that above analysis is only valid when the origin  $(0, 0)$  is not on the zero level set of  $\psi$  because  $\psi$  is not  
 91 differentiable at points where  $\psi = 0$ . If  $\psi$  is constant along the normal direction of the front (*i.e.*,  $\psi_{0,1} = 0$ ),  
 92 the leading order behavior of the front motion is  $g^{(2)}$  which denotes mean curvature. This reduces to the  
 93 formal analysis to the original MBO method [35].

94 Now, we consider the case where the front is perturbed from the zero level set of  $\psi$  and assume  $\psi_{0,0} \sim O(\varepsilon)$   
 95 and  $\psi_{0,1} \sim O(1)$ . Then, the value of  $\tilde{x}_2$  (the velocity of the front) is dominated by  $-2\psi_{0,1}$ . Therefore, every  
 96 point on the front moves to the direction which decreases the value of  $\psi$  (see, for example, a diagram in  
 97 Figure 2). Since  $\psi = |d|^{p/2}$ , in the leading order, the front evolves to  $\psi = 0$ .

98 *Remark 3.1.* We remark here that the above analysis only gives the formal leading order velocity of motion  
 99 of the front. In (19), there is still one term regarding the mean curvature which may play an important  
 100 role when  $\psi_{0,0}$  is not small (*i.e.*, the front is far away from the point cloud). This observation gives several  
 101 suggestions on the setting of the algorithms: 1.) The initial guess should contain the point cloud and 2.)  
 102 the initial choice  $\tau$  should not be very large, otherwise, the front evolves to the global minimizer  $\emptyset$  except  
 103 the local minimizer.

104 *Remark 3.2.* All above computation can be done for Algorithm 1 similarly.

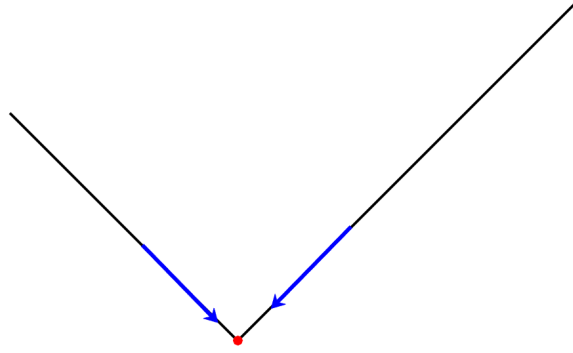


Figure 2: A diagram for the direction of motion of the front. See Section 3.

#### 105 4. Accelerations on Algorithms 1 and 2.

106 As we mentioned in Section 3, both Algorithm 1 and Algorithm 2 are related to interface dynamics and  
 107  $\tau$  is a free parameter which can be interpreted as the time step. Because the method is unconditional stable  
 108 as shown in Section 2.3, the algorithms work for any large  $\tau$ . However,  $\tau$  is also related to the approximation  
 109 of the energy functional. We do need to use small  $\tau$  to obtain a good approximation. In the discrete case,  
 110 when the domain  $\Omega$  is discretized by a uniform mesh, the interface may stuck with a small  $\tau$ , where the  
 111 indicator functions between two iterations are exactly same. The whole algorithm is then stuck.

112 Based on above observations, we propose to accelerate Algorithms 1 and 2 with building a sequence  
 113  $\tau_1 > \tau_2 > \tau_3 > \dots > \tau_N$ . We start with solving Algorithms 1 and 2 with  $\tau_1$  until convergence and then we  
 114 use the obtained solution to build an initial guess of the Algorithms with  $\tau_2$ . This is repeated until we have  
 115 obtained two exactly same solutions with  $\tau_\ell$  and  $\tau_{\ell+1}$ . The algorithm is summarized into Algorithm 3.

---

**Algorithm 3:** The accelerated version of Algorithm 1 or 2.

---

**Input:**  $\Omega$ : computational domain;  $d(\mathbf{x})$ : distance function to the point cloud; a sequence

$$\tau_1 > \tau_2 > \tau_3 > \dots > \tau_N; \tau = \tau_1; s = 1; \text{ and } u^0 \in \mathcal{B}.$$

**Output:**  $u^* \in \mathcal{B}$ .

**while** *not converged* **do**

Run Algorithm 1 or 2 to obtain the stationary solution  $u^*$  at current  $\tau$ .

$s = s + 1$

$\tau = \tau_s$

---

116 *Remark 4.1.* We remark here that  $\tau_1, \tau_2, \dots$  are not required to be chosen specifically or initially. One could  
 117 simply choose  $\tau_{s+1} = \frac{\tau_s}{2}$  each time after the algorithms with  $\tau_s$  converges.

118 The advantages of Algorithm 3 can be understood as follows:

- 119 1. It avoids the solution to be stuck.  
 120 2. The initial large  $\tau$  makes the solution converge faster.  
 121 3. Algorithm 3 converges at the a relatively small  $\tau$ , which guarantees the accuracy of the solution.

## 122 5. Numerical implementation and experiments

### 123 5.1. Numerical implementation

In this section, we discuss the implementation of the whole algorithm. When the point cloud is fixed,  $d(\mathbf{x})$  is fixed and only needs to be evaluated once. That is, from the point cloud  $\mathcal{C}$ , we expect to solve

$$\begin{cases} |\nabla d| = 1, & \mathbf{x} \in \Omega, \\ d(\mathbf{x}) = 0, & \mathbf{x} \in \mathcal{C}. \end{cases} \quad (20)$$

Following [36], we simply choose a first order Lax–Friedrich scheme to discretize the relaxed dynamical equation of (20):

$$d_{i,j}^{n+1} = \frac{1}{2} \left( 1 - |\nabla d_{i,j}^n| + \frac{d_{i+1,j}^n + d_{i-1,j}^n}{2} + \frac{d_{i,j+1}^n + d_{i,j-1}^n}{2} \right) \quad (21)$$

124 and use a fast sweeping method [37] to solve it with a linear complexity.

125 Because the point cloud is discrete, if one plots the  $\varepsilon$ -level set (relatively small  $\varepsilon$ ) of the computed  
 126  $d(\mathbf{x})$ , the contours are small circles around each points in the cloud (see Figure 3). Figure 3 tells that a  
 127 distance function computed from discrete point cloud does not imply the surface reconstruction from point  
 128 cloud, especially in high dimensional cases where the ordering of points are much more complicated than  
 129 2-dimensional cases. That’s the reason that we consider minimizing the objective function to obtain the  
 130 reconstructed surface instead of direct interpolation from the computed distance function.

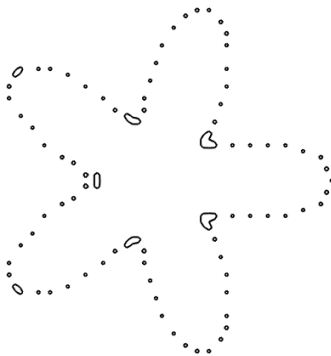


Figure 3: A diagram for a  $\varepsilon$ -level set of the distance function computed from (20). See Section 5.1.

131 Besides above, we only need to compute convolutions in each iteration. They are efficiently computed  
 132 using fast Fourier transform (FFT) based on a uniformly discretized computational domain.

133 *5.2. Numerical experiments.*

134 In this section, we provide a variety of numerical experiments to show the performance of the proposed  
 135 algorithm. We implemented all algorithms in MATLAB. All reported results were obtained on a laptop  
 136 with a 2.7GHz Intel Core i5 processor and 8GB of RAM. In all experiments, the domain  $\Omega = [-\pi, \pi]^n$  is  
 137 discretized with uniform meshes. If there is no other statement, the CPU time we report is the total CPU  
 138 time for iterations after  $d(\mathbf{x})$  is computed and  $p = 2$ . For the convenience, we denote Algorithm 3.1 (or 3.2)  
 139 as Algorithm 3 cooperated with Algorithm 1 (or 2).

140 *5.2.1. Comparisons between Algorithms 1- 3.*

In this section, we perform several experiments to show the comparisons among Algorithms 1-3. We use two point clouds in this experiment as displayed in Figure 4. The 2-dimensional point cloud is generated using  $N = 200$  uniform grids  $\theta_i$  ( $i \in [N]$ ) in  $[0, 2\pi]$ :

$$\begin{cases} x_i = r_i \cos(\theta_i), \\ y_i = r_i \sin(\theta_i) \end{cases}$$

where  $r_i = 1 + 0.5 \cos(5(\theta_i - \pi/2))$ . The 3-dimensional point cloud is generated from  $N = 2000$  random points  $(u_i, v_i)$ ,  $i \in [N]$  (i.i.d. from uniform distribution) in  $[0, 2\pi]^2$  by:

$$\begin{cases} x_i = (1 + 0.5 \cos(u_i)) \cos(v_i), \\ y_i = (1 + 0.5 \cos(u_i)) \sin(v_i), \\ z_i = 0.5 \sin(u_i). \end{cases}$$

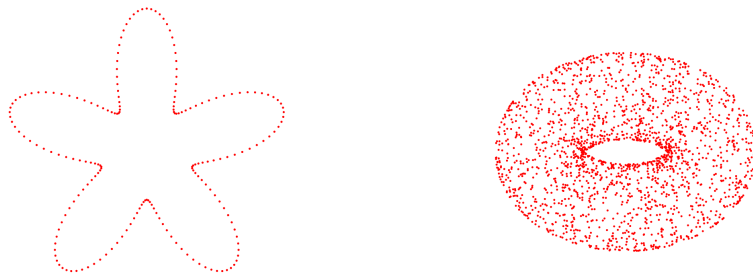


Figure 4: **Left:** Point cloud of five folds. **Right:** Point cloud of a torus. See Section 5.2.1.

141 Figure 5 displays results from Algorithms 1 and 2 with different values of  $\tau$  for the 2-dimensional point  
 142 cloud. Figure 6 displays the results obtained using Algorithms 3.1 and 3.2. In Figure 5, for a small  
 143  $\tau = 0.0025$ , the solution is stuck at an incorrect solution which is just because of the spatial discretization.  
 144 In Algorithm 3, this is easily avoided by using the adaptive in time strategy. In all experiments, the  
 145 computational domain  $[-\pi, \pi]^2$  is discretized by  $128^2$  uniform grids.

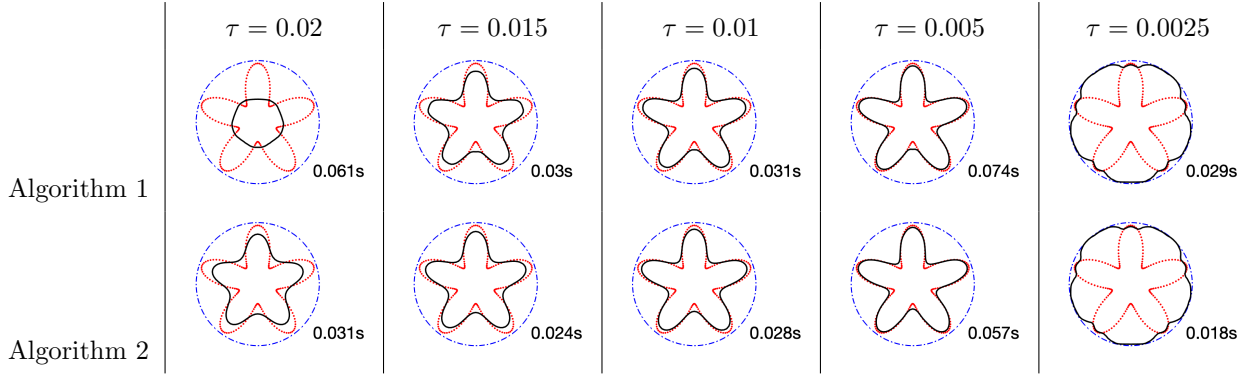


Figure 5: **First row:** Computed results from Algorithm 1 with different  $\tau$ . **Second row:** Computed results from Algorithm 2 with different  $\tau$ . **Blue curves:** Initial guess. **Black curves:** Reconstructed surface. See Section 5.2.1.

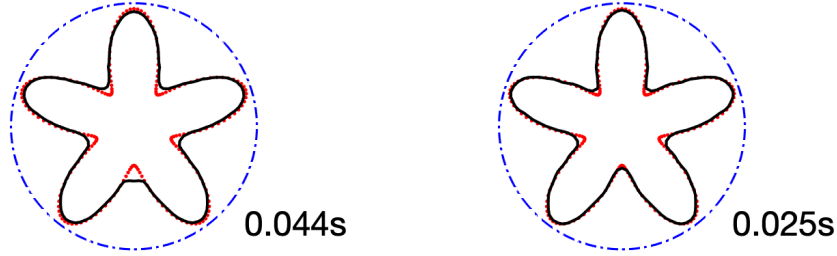


Figure 6: **Left:** The result computed with Algorithm 3.1. **Right:** The result computed with Algorithm 3.2. The  $\tau_i$  used in both experiments are 0.02, 0.01, 0.005, 0.0025, and 0.00125; respectively. See Section 5.2.1.

Figure 7 displays the 3-dimensional results obtained from Algorithms 1 and 2 with different choices of  $\tau$ . In all experiments, the initial guess is simply set to be the indicator function of a rectangular box:

$$\{(x, y, z) : |x| < 1.6, |y| < 1.6, \text{ and } |z| < 0.6\}.$$

146 The computational domain  $[-\pi, \pi]^3$  is discretized with  $128^3$  uniform grids. It's easy to see that small  $\tau$   
 147 makes both Algorithms stuck at some local minimizers of the discretized problem. However, smaller  $\tau$  does  
 148 give a closer surface to the point cloud. In Figure 8, we list the results obtained from Algorithm 3.1 and  
 149 2. Visually, the surfaces reconstructed from Algorithm 3 are much better than the results in Figure 7,  
 150 respectively. From above two experiments, we observe that Algorithm 3 is more accurate and robust than  
 151 Algorithms 1 and 2.

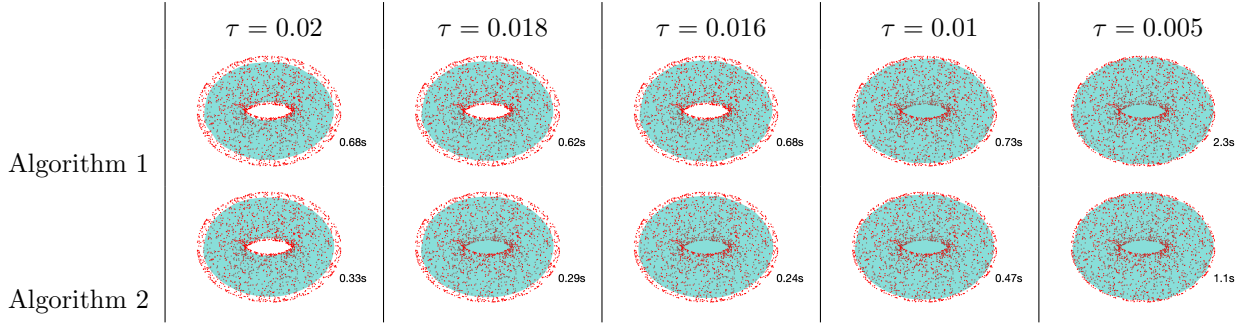


Figure 7: **1st row:** Computed results from Algorithm 1 with different  $\tau$ . **2nd row:** Computed results from Algorithm 2 with different  $\tau$ . See Section 5.2.1.

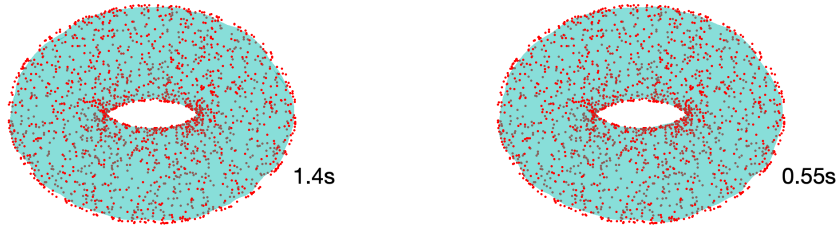


Figure 8: **Left:** The result computed with Algorithm 3.1. **Right:** The result computed with Algorithm 3.2. The  $\tau_i$  ( $i = 1, 2, 3, 4$ ) used in both experiments are 0.02, 0.01, 0.005, and 0.0025; respectively. See Section 5.2.1.

### 152 5.2.2. The energy decaying property.

In this section, we show the energy decaying property (especially on Algorithm 3) via a 2-dimensional three-fold example. The point cloud is generated using  $N = 100$  uniform points  $\theta_i$  in  $[0, 2\pi]$ :

$$\begin{cases} x_i = r_i \cos(\theta_i), \\ y_i = r_i \sin(\theta_i) \end{cases}$$

153 where  $r_i = 1 + 0.5 \cos(3(\theta - \pi/2))$ .

154 Figure 9 displays the energy decaying curves of Algorithms 1 and 2. Even we only have the theoretical  
 155 proof of the energy decaying property for Algorithm 2, numerical experiments indicate that Algorithm 1  
 156 also has the energy decaying property. In both figures, for different choices of  $\tau$ , the curves have similar  
 157 profiles with only sketching (or compressing) along the  $x$ -axis (number of iterations). This is also consistent  
 158 with the fact that  $\tau$  plays the role of time step in the algorithm for the dynamics of the contour, as we  
 159 discussed in Section 3.

160 Figure 10 displays energy decaying curves during iterations for Algorithm 3.1 and 3.2. In both figures,  
 161 relatively big jumps occur at the iteration when  $\tau$  is changed. Several snapshots at the jumps are shown in  
 162 both figures. From Figure 10, we observe that the initially choice of  $\tau$  (relatively large) can quickly give a  
 163 solution in the regime of the local minimizer and smaller  $\tau$  refines the solution.

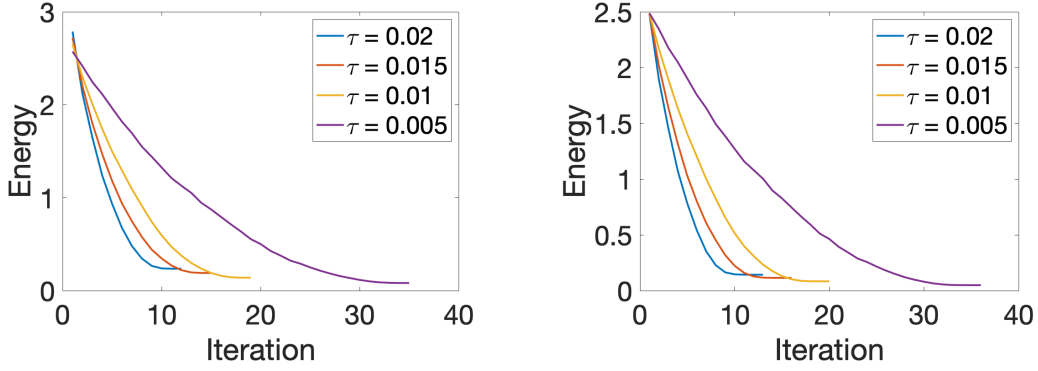


Figure 9: Energy decaying curves for Algorithms 1 and 2 (**left:** Algorithm 1, **right:** Algorithm 2). See Section 5.2.2.

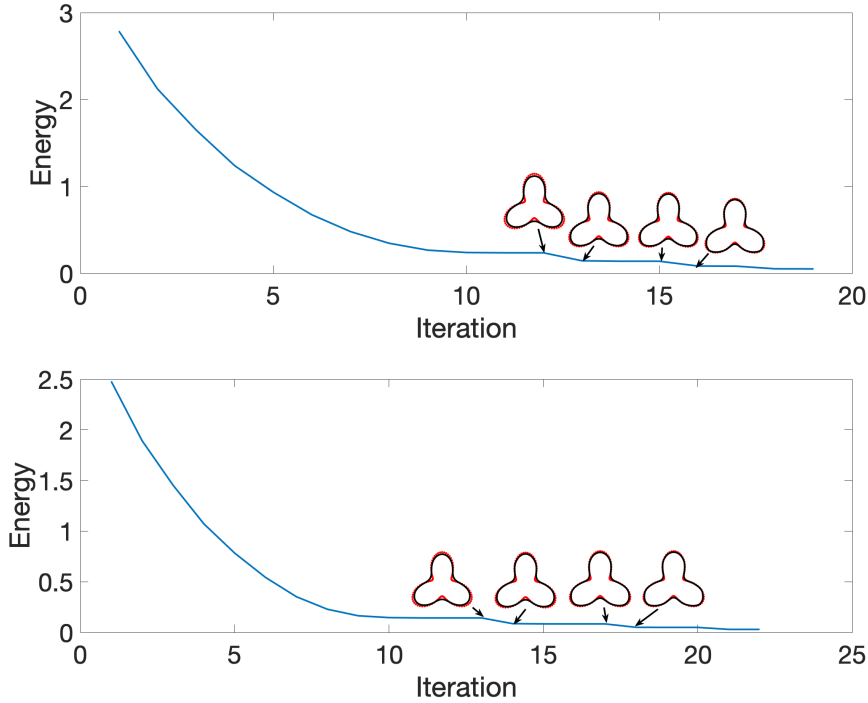


Figure 10: Energy decaying curves for Algorithms 3.1 and 3.2 (**top:** Algorithm 3.1, **bottom:** Algorithm 3.2). See Section 5.2.2.

### 164 5.2.3. Sensitivity to $p$ .

165 In this experiment, we check the dependency of the results on the value of  $p$ . In Figure 11, we list  
 166 the results obtained from Algorithm 3.2 for different choices of  $p$ . The values of  $p$  used in Figure 11 are  
 167 1, 2, 3, 4, and 5 from the left to the right, respectively. We observe that for  $p \geq 2$ , the results show little  
 168 difference. However, the result obtained from Algorithm 3.2 using  $p = 1$  deviates a little from the correct  
 169 curve. Actually, we did a lot similar experiments for different types of point clouds with different values of  
 170  $p$ , the behavior of the solutions are similar as those in Figure 11. In other words,  $p = 1$  gives worse results

171 from our numerical observation. This is reasonable because  $|d|^{p/2}$  is not Lipschitz on the front when  $p = 1$ .

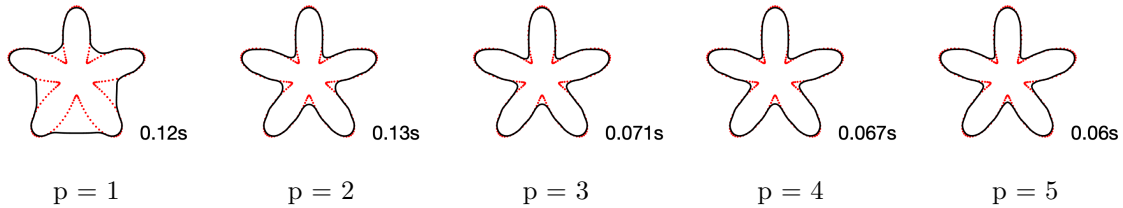


Figure 11: Results obtained from Algorithm 3.2 using different values of  $p$ . **Left to right:**  $p = 1, 2, 3, 4,$  and  $5$ . See Section 5.2.3.

#### 172 5.2.4. Sensitivity to noisy data.

173 In this experiment, we perform several experiments to show the capability of proposed algorithms in noisy  
 174 data. Because Algorithm 3 gives better results than Algorithms 1 and 2, in the following and subsequent  
 175 experiments, we only show results from Algorithm 3.2.

176 We consider the noisy data  $\tilde{\mathbf{x}}$  generated from the pure data  $\mathbf{x}$ :  $\tilde{\mathbf{x}} = \mathbf{x} + \mu\nu$ , where  $\nu$  is a vector whose  
 177 entries are independently and identically distributed random variables from a normal distribution and  $\mu$  is  
 178 a parameter to control the intensity of noise. In Figure 12, we observe that the method still works for noisy  
 179 data, especially when the noise intensity is not very high. In addition, the two-circle case indicates that  
 180 the algorithm works well for topological changing cases. In these experiments, the computational domain  
 181  $[-\pi, \pi]^2$  is discretized by  $128^2$  grids.

#### 182 5.2.5. Sensitivity to resolutions.

183 In this experiment, we check the sensitivity of the proposed algorithms to the resolution of the com-  
 184 putational domain and the number of the point cloud. In Figure 13, we list the results obtained from  
 185 Algorithm 3.2, using different discretization of the computational domain and different size of the point  
 186 cloud. In Figure 3, the size of point clouds from the left to the right are 100, 200, 300, and 400, respectively.  
 187 The computational domains from the top to the bottom are discretized by  $64^2$ ,  $128^2$ ,  $256^2$ , and  $512^2$  grids.  
 188 We observe that as the mesh is refined, the result is closer to the desired curve. In addition, point clouds  
 189 with larger size can give better results. These agree with our expectations.

#### 190 5.2.6. Efficiency comparison with level set approaches.

In this example, we compare the efficiency between Algorithm 3.2 and level set approaches. A recent  
 work in [36] has carefully studied the efficiency comparison between the semi-implicit method (SIM) and  
 the classic level set approach in [7], showing great improvement in the efficiency. Therefore, in this section,  
 we simply compare the efficiency between Algorithm 3.2 and SIM in [36]. We consider different point clouds

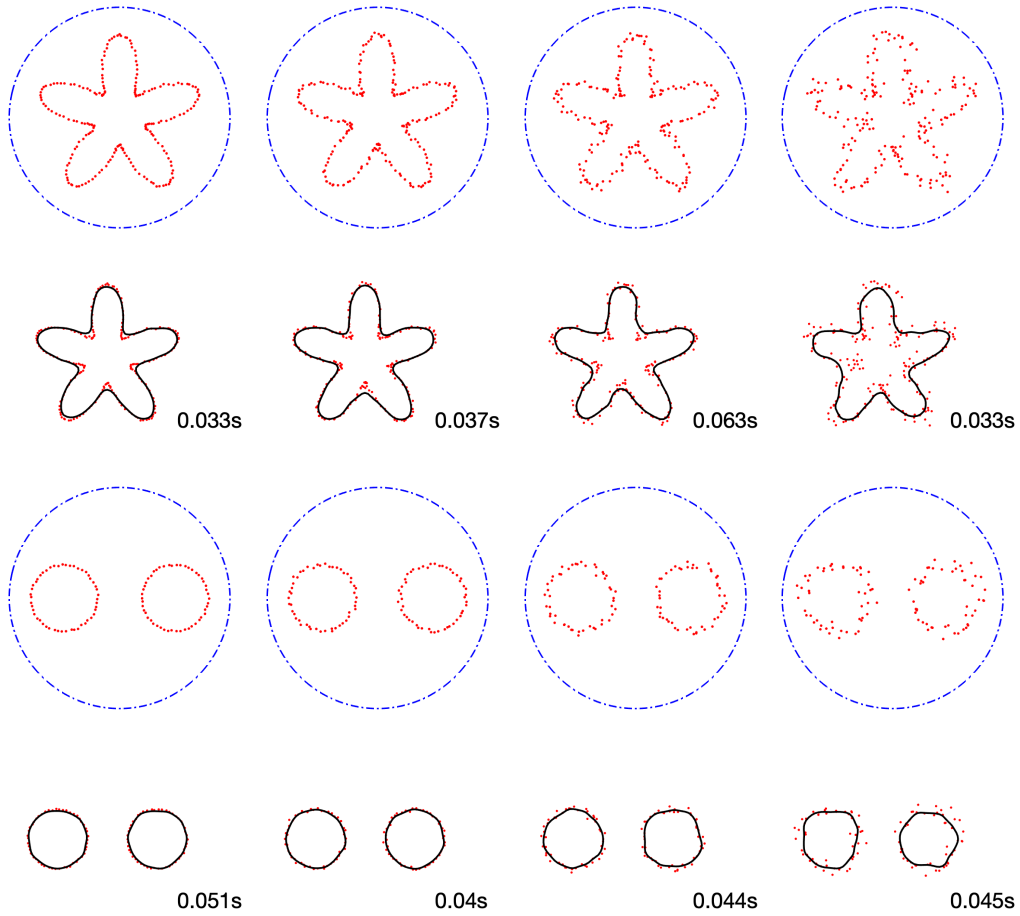


Figure 12: Results obtained for the five-fold data with different noise. **Left to right:**  $\mu = 0.01, 0.02, 0.04, 0.08$ . **1st and 3rd row:** Noisy data with the initial guess. **2nd and 4th row:** Results obtained from Algorithm 3.2. See Section 5.2.4.

(different  $m$ ) generated using  $N = 200$  uniform points  $\theta_i$  in  $[0, 2\pi]$ :

$$\begin{cases} x_i = r_i \cos(\theta_i), \\ y_i = r_i \sin(\theta_i), \end{cases}$$

191 where  $r_i = 1 + 0.4 \sin(m\theta_i)$ ; see Figure 14 for the cases when  $m = 3, 4, 5, 6, 7$ , and 8. To make the  
 192 comparison fair, we use the same initial guess as shown in Figure 14 and same discretization ( $128^2$  grids)  
 193 of the computational domain. The table shows the dramatical acceleration in the computational CPU time  
 194 and figures indicate the improvement on the accuracy.

### 195 5.2.7. 3-dimensional examples.

196 In the last example, we show the performance of the proposed algorithms in reconstructing 2-dimensional  
 197 surface from the 3-dimensional point cloud. In the follows, we choose the  $\sigma$ -level set from  $d(\mathbf{x})$  as the initial

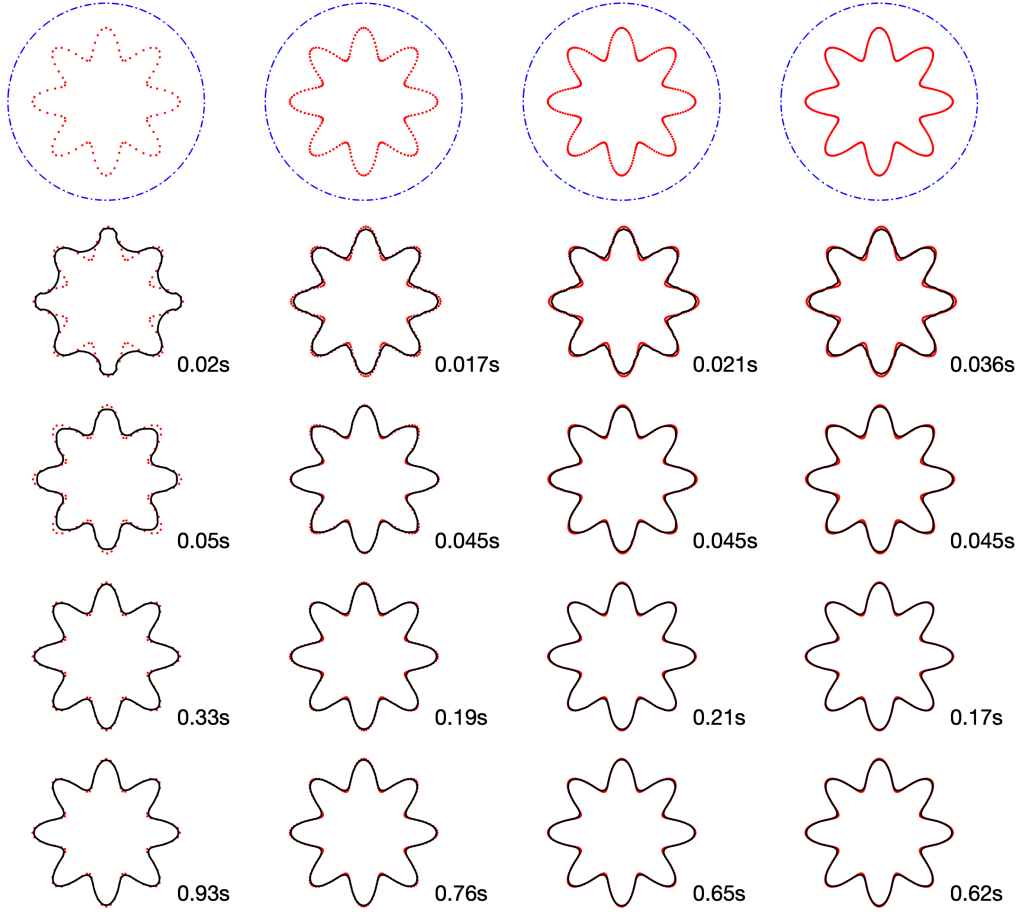
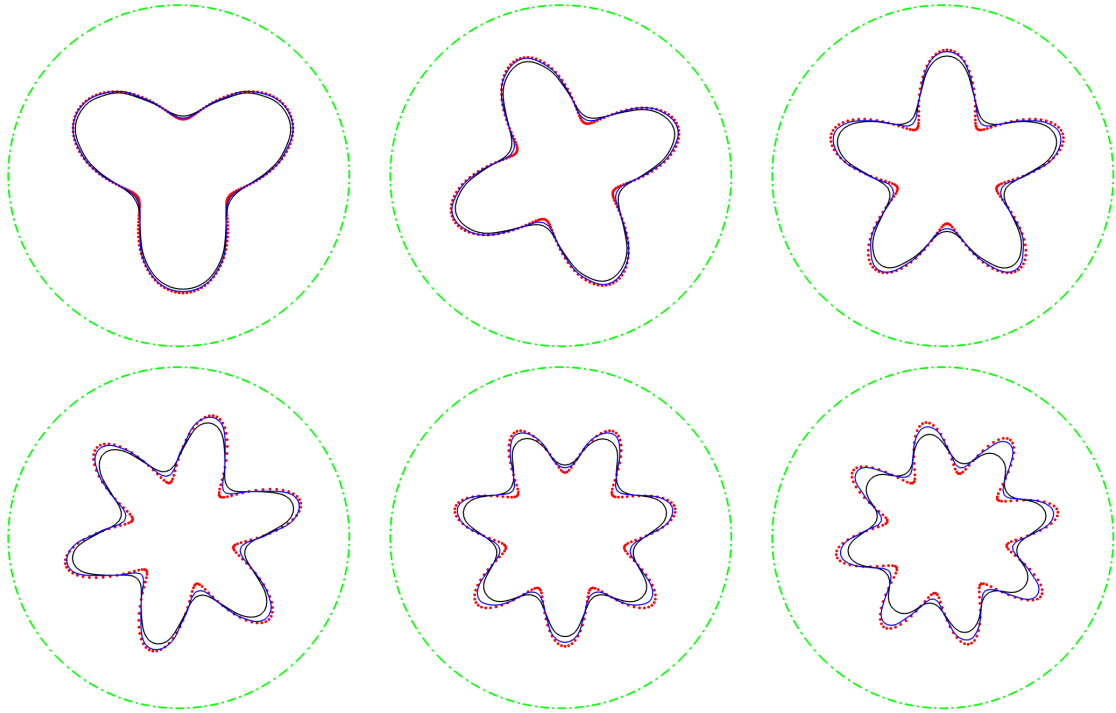


Figure 13: Results obtained from Algorithm 3 using different discretization of the computational domain and different sizes of point clouds. **Top to bottom:** Computational domain discretized by  $64^2$ ,  $128^2$ ,  $256^2$ , and  $512^2$  grids. **Left to right:** Point clouds with 100, 200, 300, and 400 points. See Section 5.2.5.

198 guess of the Algorithm with a relatively large  $\sigma$ . We note that  $\sigma$  can not be very small because the  $\sigma$ -level  
 199 set are then small balls around each point, similar to those in Figure 3.

200 Figure 15 displays the reconstructed results from different point clouds: noisy torus, two tori, bumpy  
 201 torus, bunny, and pig. The computational domain  $[-\pi, \pi]^3$  is discretized by  $128^3$  grids. We observe that for  
 202 most parts in these point clouds, they are well reconstructed especially when the curvature is not that big.  
 203 However, when the curvature is very big, it is very difficult to touch (*e.g.*, the ears of the bunny and pig)  
 204 because of the diffusion effect. This is consistent with the dynamical motion law we derived in Section 3. We  
 205 expect that this could be improved by considering some more terms (for example, a curvature term as that  
 206 in [38]) in the objective energy. The CPU time of each experiment is printed on each figure respectively. All  
 207 of them are done in seconds on  $128^3$  grids, indicating the efficiency of the method.



SIM in [36]	3.2 s	4.47 s	5.26 s	6.40 s	7.18 s	4.56 s
Algorithm 3.2	0.029 s	0.036 s	0.029 s	0.026 s	0.031 s	0.030 s

Figure 14: Comparisons between Algorithm 3.2 and SIM in [36]. **Blue curve:** results obtained from Algorithm 3. **Black curve:** results obtained from SIM in [36]. **Green curve:** initial guess. **Red points:** point cloud with 200 points. **Table:** CPU times for the computations. See Section 5.2.6.

## 208 6. Conclusion and discussions

209 In this paper, we developed a novel iterative method to minimize an objective energy functional to  
 210 reconstruct codimension-1 surfaces from point clouds in both 2- and 3-dimensional Euclidean spaces. The  
 211 method is simple and unconditional stable in the sense of energy decaying. We carefully checked the  
 212 properties and efficiency using a variety of numerical experiments. The proposed algorithms show great  
 213 advantages than the level set approaches.

214 From numerical experiments, we observe that thin parts with large curvature are difficult to reconstruct,  
 215 especially for 3-dimensional point clouds. We expect this could be improved by considering more terms in  
 216 the objective functional and this will be investigated and reported in the future. As for the Algorithm 1,  
 217 even all numerical results we performed so far imply the unconditional stability, the theoretical proof is still  
 218 needed which we believe requires new mathematical tools. Since the surfaces are represented by indicator  
 219 functions, the accuracy is dependent on the resolution of the discretization mesh. One could use a multi-  
 220 scale strategy to refine the mesh after obtaining the results on a coarse mesh and set the results as the

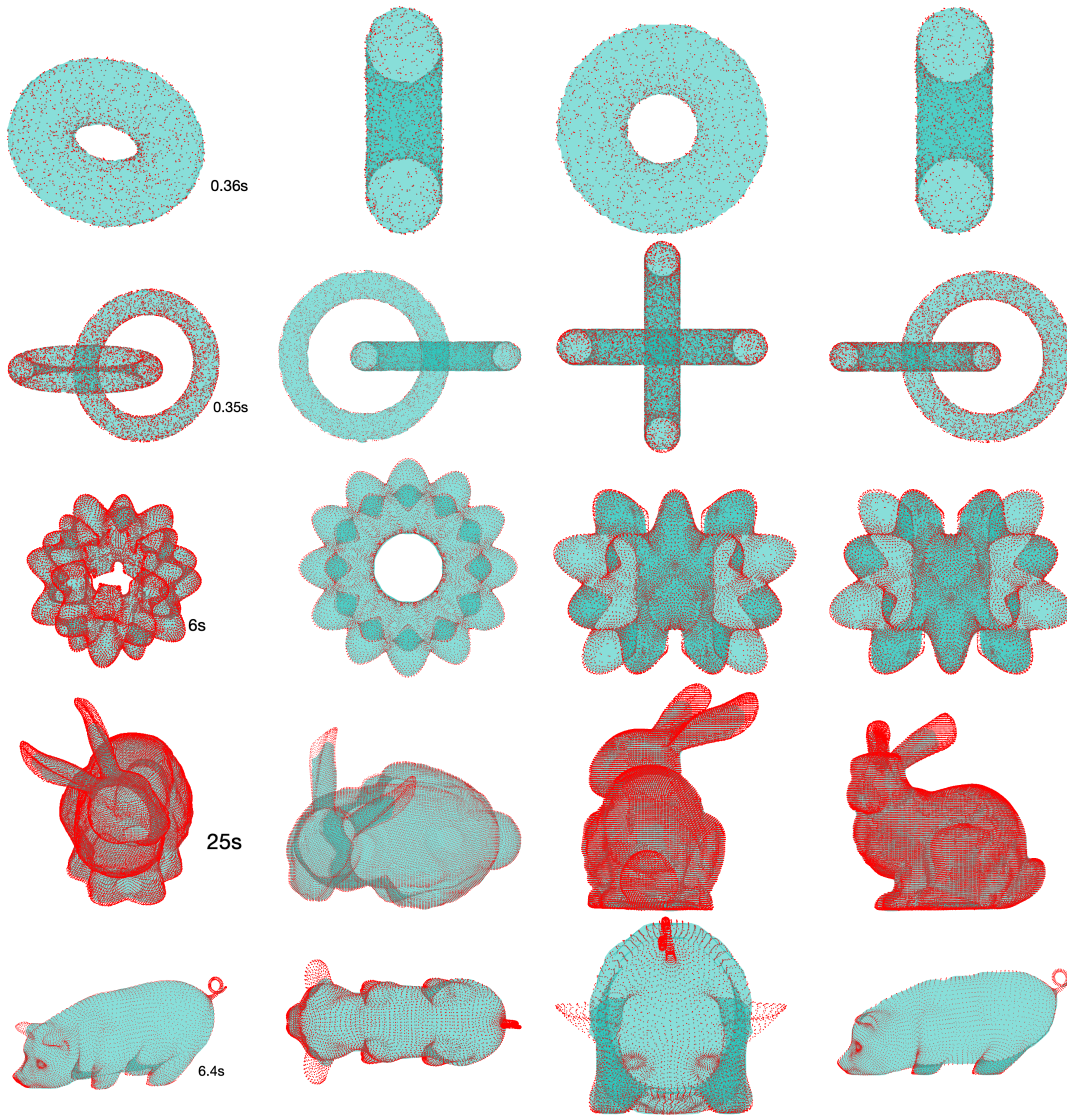


Figure 15: Results obtained from Algorithm 3.2. **Left to right:** Reconstructed surface from point cloud,  $xy$ -view,  $yz$ -view, and  $xz$ -view. See Section 5.2.7.

221 initial condition of the refined mesh. In addition, for those applications requiring finer design, the proposed  
 222 methods can be used as an efficient tool for initialization which can be directly cooperated with a high order  
 223 accurate method.

224 The CPU time for both 2- and 3-dimensional experiments have clearly shown the fast convergence of the  
 225 algorithm. One could directly extend all proposed algorithms to higher dimensional problems.

#### 226 *Acknowledgements*

227 The author would like to thank Wei Hu, Hao Liu, and Jun Ma for helpful discussions. The author would  
 228 also like to thank Xiao-Ping Wang and Braxton Osting for constant support, help and encouragement.

229 **References**

- 230 [1] R. Bolle, B. Vemuri, On three-dimensional surface reconstruction methods, *IEEE Transactions on Pattern Analysis and*  
 231 *Machine Intelligence* 13 (1) (1991) 1–13. doi:10.1109/34.67626.
- 232 [2] Y. Wang, Characterizing three-dimensional surface structures from visual images, *IEEE Transactions on Pattern Analysis*  
 233 *and Machine Intelligence* 13 (1) (1991) 52–60. doi:10.1109/34.67630.
- 234 [3] F. Calakli, G. Taubin, SSD: Smooth signed distance surface reconstruction, *Computer Graphics Forum* 30 (7) (2011)  
 235 1993–2002. doi:10.1111/j.1467-8659.2011.02058.x.
- 236 [4] D. Khan, M. A. Shirazi, M. Y. Kim, Single shot laser speckle based 3d acquisition system for medical applications, *Optics*  
 237 *and Lasers in Engineering* 105 (2018) 43–53. doi:10.1016/j.optlaseng.2018.01.001.
- 238 [5] Z. Bi, L. Wang, Advances in 3d data acquisition and processing for industrial applications, *Robotics and Computer-*  
 239 *Integrated Manufacturing* 26 (5) (2010) 403–413. doi:10.1016/j.rcim.2010.03.003.
- 240 [6] M. Berger, A. Tagliasacchi, L. M. Seversky, P. Alliez, G. Guennebaud, J. A. Levine, A. Sharf, C. T. Silva, A survey of  
 241 surface reconstruction from point clouds, *Computer Graphics Forum* 36 (1) (2016) 301–329. doi:10.1111/cgf.12802.
- 242 [7] H.-K. Zhao, S. Osher, B. Merriman, M. Kang, Implicit and nonparametric shape reconstruction from unorganized data  
 243 using a variational level set method, *Computer Vision and Image Understanding* 80 (3) (2000) 295–314. doi:10.1006/  
 244 *cviu.2000.0875*.
- 245 [8] M. Kazhdan, M. Bolitho, H. Hoppe, Poisson surface reconstruction, in: *Proceedings of the fourth Eurographics symposium*  
 246 *on Geometry processing*, Eurographics Association, 2006, pp. 61–70.
- 247 [9] A. C. Öztireli, G. Guennebaud, M. Gross, Feature preserving point set surfaces based on non-linear kernel regression,  
 248 *Computer Graphics Forum* 28 (2) (2009) 493–501. doi:10.1111/j.1467-8659.2009.01388.x.
- 249 [10] H. Q. Dinh, G. Turk, G. Slabaugh, Reconstructing surfaces using anisotropic basis functions, in: *Proceedings Eighth IEEE*  
 250 *International Conference on Computer Vision. ICCV 2001, Vol. 2, IEEE, 2001*, pp. 606–613.
- 251 [11] L. Nan, P. Wonka, PolyFit: Polygonal surface reconstruction from point clouds, in: *2017 IEEE International Conference*  
 252 *on Computer Vision (ICCV), IEEE, 2017*, pp. 2372–2380. doi:10.1109/iccv.2017.258.
- 253 [12] J. Liang, F. Park, H. Zhao, Robust and efficient implicit surface reconstruction for point clouds based on convexified image  
 254 segmentation, *Journal of Scientific Computing* 54 (2-3) (2012) 577–602. doi:10.1007/s10915-012-9674-8.
- 255 [13] B. Merriman, J. K. Bence, S. Osher, Diffusion generated motion by mean curvature, Department of Mathematics, Uni-  
 256 versity of California, Los Angeles, 1992. doi:ftp://ftp.math.ucla.edu/pub/camreport/cam92-18.pdf.
- 257 [14] B. Merriman, J. Bence, S. Osher, Diffusion generated motion by mean curvature, *AMS Selected Letters, Crystal Grower’s*  
 258 *Workshop* (1993) 73–83.
- 259 [15] B. Merriman, J. K. Bence, S. J. Osher, Motion of multiple junctions: A level set approach, *Journal of Computational*  
 260 *Physics* 112 (2) (1994) 334–363. doi:10.1006/jcph.1994.1105.
- 261 [16] S. Esedoglu, F. Otto, Threshold dynamics for networks with arbitrary surface tensions, *Communications on Pure and*  
 262 *Applied Mathematics* 68 (5) (2014) 808–864. doi:10.1002/cpa.21527.
- 263 [17] S. J. Ruuth, B. T. Wetton, A simple scheme for volume-preserving motion by mean curvature, *Journal of Scientific*  
 264 *Computing* 19 (1-3) (2003) 373–384. doi:10.1023/A:1025368328471.
- 265 [18] M. Jacobs, E. Merkurjev, S. Esedoglu, Auction dynamics: A volume constrained MBO scheme, *Journal of Computational*  
 266 *Physics* 354 (1) (2018) 288–310. doi:10.1016/j.jcp.2017.10.036.
- 267 [19] X. Xu, D. Wang, X.-P. Wang, An efficient threshold dynamics method for wetting on rough surfaces, *Journal of Compu-*  
 268 *tational Physics* 330 (1) (2017) 510–528. doi:10.1016/j.jcp.2016.11.008.
- 269 [20] D. Wang, X.-P. Wang, X. Xu, An improved threshold dynamics method for wetting dynamics, *Journal of Computational*  
 270 *Physics* 392 (2019) 291–310. doi:10.1016/j.jcp.2019.04.037.

- 271 [21] S. Esedoglu, Y.-H. R. Tsai, et al., Threshold dynamics for the piecewise constant mumford–shah functional, *Journal of*  
272 *Computational Physics* 211 (1) (2006) 367–384. doi:10.1016/j.jcp.2005.05.027.
- 273 [22] E. Merkurjev, T. Kostic, A. L. Bertozzi, An MBO scheme on graphs for classification and image processing, *SIAM Journal*  
274 *on Imaging Sciences* 6 (4) (2013) 1903–1930. doi:10.1137/120886935.
- 275 [23] D. Wang, H. Li, X. Wei, X.-P. Wang, An efficient iterative thresholding method for image segmentation, *Journal of*  
276 *Computational Physics* 350 (1) (2017) 657–667. doi:10.1016/j.jcp.2017.08.020.
- 277 [24] D. Wang, X.-P. Wang, The iterative convolution-thresholding method (ictm) for image segmentation, arXiv preprint  
278 arXiv:1904.10917.
- 279 [25] B. Osting, D. Wang, A diffusion generated method for orthogonal matrix-valued fields, *Mathematics of Computation* 89  
280 (2020) 515 – 550. doi:10.1090/mcom/3473.
- 281 [26] D. Wang, B. Osting, X.-P. Wang, Interface dynamics for an allen-cahn-type equation governing a matrix-valued field,  
282 *SIAM Journal on Multiscale Modeling and Simulation* 17(4) (2019) 1252–1273. doi:10.1137/19M1250595.
- 283 [27] D. Wang, B. Osting, A diffusion generated method for computing Dirichlet partitions, *Journal of Computational and*  
284 *Applied Mathematics* 351 (2019) 302–316. doi:10.1016/j.cam.2018.11.015.
- 285 [28] B. Osting, , D. Wang, Diffusion generated methods for denoising target-valued images, *Inverse Problems & Imaging* 14 (2)  
286 (2020) 205–232. doi:10.3934/ipi.2020010.
- 287 [29] S. Esedoglu, R. Tsai, S. Ruuth, Threshold dynamics for high order geometric motions, *Interfaces and Free Boundaries*  
288 (2008) 263–282doi:10.4171/ifb/189.
- 289 [30] B. Merriman, S. J. Ruuth, Convolution-generated motion and generalized Huygens’ principles for interface motion, *SIAM*  
290 *Journal on Applied Mathematics* 60 (3) (2000) 868–890. doi:10.1137/S003613999833397X.
- 291 [31] S. J. Ruuth, B. Merriman, Convolution–thresholding methods for interface motion, *Journal of Computational Physics*  
292 169 (2) (2001) 678–707. doi:10.1006/jcph.2000.6580.
- 293 [32] M. Elsey, S. Esedoglu, Threshold dynamics for anisotropic surface energies, *Mathematics of Computation* 87 (312) (2017)  
294 1721–1756. doi:10.1090/mcom/3268.
- 295 [33] M. Miranda, D. Pallara, F. Paronetto, M. Preunkert, Short-time heat flow and functions of bounded variation in  $\mathbb{R}^n$ ,  
296 *Annales de la faculté des sciences de Toulouse Mathématiques* 16 (1) (2007) 125–145. doi:10.5802/afst.1142.
- 297 [34] W. Hu et al, ———, preprint.
- 298 [35] P. Mascarenhas, Diffusion generated motion by mean curvature, department of Mathematics, University of California, Los  
299 Angeles (1992).
- 300 [36] Y. He, M. Huska, S. H. Kang, H. Liu, Fast algorithms for surface reconstruction from point cloud, arXiv preprint  
301 arXiv:1907.01142.
- 302 [37] C. Y. Kao, S. Osher, J. Qian, Lax–friedrichs sweeping scheme for static hamilton–jacobi equations, *Journal of Computa-*  
303 *tional Physics* 196 (1) (2004) 367–391. doi:10.1016/j.jcp.2003.11.007.
- 304 [38] Y. He, S. H. Kang, H. Liu, Curvature regularized surface reconstruction from point cloud, arXiv preprint arXiv:2001.07884.